Additive-manufactured topology-optimized heat sinks for enhancing thermoelectric generator conversion efficiency

Junyoung Park[1], Hyun Yu[1], Ki Mun Bang[1], Woochul Kim[2], Hyungyu Jin[1,3*]

[1]*Department of Mechanical Engineering, Pohang University of Science and Technology (POSTECH), Pohang 37673, South Korea*

[2]*School of Mechanical Engineering, Yonsei University, Seoul 03722, South Korea*

[3]*Institute for Convergence Research and Education in Advanced Technology, Yonsei University, Seoul 037, South Korea*

*Corresponding author

E-mail address: hgjin@postech.ac.kr (H. Jin)

Abstract

Thermoelectric generators (TEGs) are gaining great attention as a promising technology for waste heat recovery due to their ability to directly convert heat into electricity. However, their relatively low conversion efficiency limits widespread adoption. While efficient thermal management of TEGs is crucial to achieve high conversion efficiencies, less attention has been paid to this aspect thus far compared to materials development. Efficient TEGs require efficient heat dissipation on the cold side of TEGs, demanding careful heat sink design. In this study, a topology optimization model was developed to design air-cooled heat sinks specifically for TEG applications, incorporating both thermoelectric properties and geometric structure of TEGs. The optimized heat sink was fabricated using additive manufacturing, and its performance was experimentally validated. Compared to a conventional rectangular fin heat sink, the topology optimized (TO) heat sink significantly reduced thermal resistance across a wide range of pressure drops (6 Pa to 30 Pa), achieving a 33.5% reduction at a 12 Pa pressure drop. This led to a 44.7% increase in the output power of a commercial TEG. Despite a ~40% increase in power consumption, the TO heat sink resulted in a 21.3% improvement in conversion efficiency. This improvement is equivalent to a 27% increase in the device thermoelectric figure of merit (*ZT*). Numerical simulations revealed that the TO heat sink can enhance temperature uniformity on the cold side of the TEG, further contributing to performance gains. These findings highlight the effectiveness of heat sink topology optimization in enhancing conversion efficiency of TEGs.

Keywords: thermoelectric generator, topology optimization, air-cooled heat sink, additive manufacturing, forced convection

Nomenclature

TEG	Thermoelectric generator
TE	Thermoelectric
$\mathbf{u}$	Fluid velocity vector
p	Pressure field (Pa)
$\mathbf{F}$	Brinkman friction coefficient
α	Maximum inverse permeability of the porous medium (s·N/m^4)
q_α, q_κ, q_h	Interpolation convexity parameter
T	Temperature (°C)
h	Heat transfer coefficient (W/m^2·K)
dz	Thickness (m)
I	Electrical current (A)
S	Device Seebeck coefficient (V/K)
R	Electrical resistance (Ω)
K	Thermal conductance (W/K)
ZT	Device thermoelectric figure of merit
q''	Heat flux (W/m^2)
Q	Heat rate (W)
P	Power (W)
$\dot{V}$	Flow rate (m^3/s)
Δp	Pressure drop (Pa)
R_{th}	Thermal resistance (K/W)
Greek symbols	
γ	Density variable
$\tilde{\gamma}$	Filtered density variable
ρ_{f}	Fluid density (kg/m^3)
c_{f}	Specific heat capacity of fluid (J/kg·K)
μ	Dynamic viscosity (Pa·s)
κ	Thermal conductivity (W/m·K)
η	Conversion efficiency (%)

1. Introduction

The rising global energy demand and the escalating climate crisis have intensified the focus on improving energy generation efficiency and increasing the production of renewable energy [1]. In the process of converting primary energy sources, such as fossil fuels, up to 70% of the input energy is typically lost as waste heat [2]. Thus, efficiently harnessing this waste heat presents a substantial opportunity to improve overall energy generation efficiency. Waste heat recovery technologies address this challenge by converting thermal energy into usable forms of energy (e.g. electrical energy, chemical energy). Among these technologies, thermoelectric generators (TEGs) have emerged as a promising solution as they can directly convert waste heat into electrical energy [3]. Unlike conventional heat engines, TEGs are solid-state devices with no moving parts, making them simpler, more reliable, and requiring low maintenance. Additionally, TEGs generate electricity without the use of fossil fuels, thereby producing no greenhouse gas emissions. These advantage s make TEGs suitable for various applications, including industrial and vehicle waste heat recovery [4–6]. However, their relatively low energy conversion efficiency and output power compared to traditional heat engines limit their broader adoption, confining their use primarily to niche markets [7].

The primary working principle of TEGs is based on the Seebeck effect, where the output voltage is proportional to the temperature difference across the device [3,7]. Consequently, the conversion efficiency and output power of TEGs increase proportional to the temperature difference between the hot and cold sides of the device. To achieve this temperature difference, TEGs are typically attached to high-temperature heat sources to keep one side of the device hot, while heat sinks are used on the opposite side to dissipate heat and maintain a cooler temperature [8–10]. In such configurations, the temperature on the cold side is primarily determined by the thermal resistance of a heat sink [11]. Therefore, the use of heat sinks with low thermal resistances, which enhance heat dissipation and increase the temperature difference, is important to achieve high conversion efficiency and output power.

Air-cooled heat sinks are commonly employed in this setup due to their reliability and compact design, which align with the advantages of TEGs [8,12,13]. In air-cooled heat sinks, convective heat transfer is the main cooling mechanism, where fin geometry plays a crucial role in determining the effectiveness of convective heat transfer by influencing fluid flow [11]. Consequently, research has focused on optimizing fin geometry in a way to reduce the thermal resistance of heat sinks, so that the power generation performance of TEGs can be enhanced [12,14–17]. However, most of previous studies thus far have been limited to modifying conventional fin geometries, typically consisting of periodic arrays of uniform rectangular fins. This limitation results in heat sinks with suboptimal cooling performance, which subsequently constrains the power generation potential of TEGs.

In other applications where heat sinks are used, topology optimization has emerged as a powerful technique that can overcome this limitation. Topology optimization is an advanced shape optimization method that allows for the design of non-intuitive, complex structures [18–20]. Borrvall et al. first introduced topology optimization as a method to optimize fluid flow for effective heat transfer [21]. Since then, this approach has been further developed and applied to various types of heat sinks, including those for natural air convection [22], forced air cooling [23,24], and liquid cooling [25,26], primarily for arbitrary or generic heat sources. Building on these generalized approaches, researchers have recently extended the use of topology-optimized (TO) heat sinks to meet specific needs, such as cooling in electronic devices [27,28], batteries [29,30], and latent heat storage systems [31]. Despite expanding research on TO heat sinks across various applications, only a few studies have experimentally validated their effectiveness [32], and none have yet applied TO heat sinks to thermoelectric (TE) power generation, leaving this area largely unexplored. Incorporating TO heat sinks in

TEGs is expected to further improve conversion efficiency and output power, resolving the aforementioned issues arising from the continued use of conventional rectangular-fin heat sink designs.

In this study, we developed and experimentally validated a topology optimization model integrated with a TEG module to design an optimized fin structure specifically for TE power generation applications. The model accounts for both the TE properties and the geometric structure of TEGs, enabling the incorporation of precise heat source boundary conditions during the topology optimization process. The TO heat sink was fabricated using additive manufacturing, and its performance was experimentally validated. Compared to a conventional rectangular fin heat sink, the TO heat sink demonstrates a significant reduction in thermal resistance over a wide range of pressure drops (6 Pa to 30 Pa). When this TO heat sink is used for a commercial TEG, its output power and conversion efficiency are increased by 44.7% and 21.3%, respectively, compared to the case where the conventional rectangular-fin heat sink is used. Numerical simulations reveal underlying mechanisms for the observed enhancement in the TO heat sink-integrated TEG.

2. Topology optimization

2.1. Topology optimization model

Since topology optimization can accommodate complex, non-intuitive geometric structures with a high degree of freedom, it requires substantial computational resources. Therefore, constructing an efficient optimization model that reduces computational cost is crucial. To address this, we employed a simplified 2D two-layer model for topology optimization, a method widely used to mitigate the high computational cost of 3D simulations [23,33]. In this model, the components of a heat sink (fins, fluid channels, and a solid base) are represented by two 2D surfaces by assuming a uniform temperature in the height direction of each component: fins and fluid channels by the top layer, and a solid base by the bottom layer. Under this assumption, heat transfer within and between the fins and fluid is modeled in the top layer, whereas heat transfer within the base plate is modeled in the bottom layer. Heat transfer between the fins and the base, as well as between the base and the fluid, is simplified to heat transfer between the two layers as shown in Fig. 1a. In this way, the computational cost of the original 3D heat transfer problem can be significantly reduced.

The primary mechanism of topology optimization for fin structure design is to determine the optimal distribution of fluid and solid domains [18]. Each domain is represented by a density variable (γ), where $\gamma = 0$ indicates a solid domain (representing the fin structure) and $\gamma = 1$ indicates a fluid domain. The fluid flow and heat transfer in the topology optimization are calculated using modified governing equations that incorporate an interpolation function $\phi(\gamma)$, with γ as a variable. Assuming an incompressible fluid, fluid dynamics are governed by the continuity equation and Navier-Stokes equation:

$$\rho_{\mathrm{f}}(\nabla \cdot \mathbf{u}) = 0 \tag{1}$$

$$\rho_f(\mathbf{u} \cdot \nabla)\mathbf{u} = -\nabla p + \mu \nabla^2 \mathbf{u} + \mathbf{F} \tag{2}$$

where ρ_f is the fluid density, $\mathbf{u}$ is the fluid velocity vector, p is the pressure field, μ is the dynamic viscosity of the fluid, and $\mathbf{F}$ is the volumetric force. In topology optimization, $\mathbf{F}$ is the Brinkman friction coefficient, set to 0 in fluid domains and a large value in solid domains to penalize fluid flow, effectively reducing fluid velocity to zero in solid regions [21]. The force $\mathbf{F}$ is defined as:

$$\mathbf{F} = -\alpha\phi_{\alpha}(\gamma)\mathbf{u} \tag{3}$$

$$\phi_{\alpha}(\gamma) = \frac{1-\gamma}{1+q_{\alpha}\gamma} \tag{4}$$

where, α is the maximum inverse permeability of the porous medium and q_α is the interpolation convexity parameter. For strong penalization, α was set to a large constant value of 10^6 s·N/m^4.

For heat transfer, the governing equation is based on the principle of energy conservation. In the top layer, where both convection and conduction occur, the governing equation is:

$$\rho_f c_f \mathbf{u}\cdot\nabla T_{top} = \nabla\cdot(\kappa_f \phi_{\kappa}(\gamma)\nabla T_{bot}) + \frac{h_f \phi_h(\gamma)(T_{bot} - T_{top})}{dz_{fin}} \tag{5}$$

where c_f is the specific heat capacity of the fluid, T_{top} is the temperature of the top layer, T_{bot} is the temperature of the bottom layer, κ_f is the thermal conductivity of the fluid, h_f is the heat transfer coefficient in the fluid domain, and dz_{fin} is the fin height. The interpolation functions $\phi_\kappa(\gamma)$ and $\phi_h(\gamma)$ are defined as:

$$\phi_{\kappa}(\gamma) = \frac{\gamma(\kappa_f(1+q_{\kappa}) - \kappa_s) + \kappa_s}{\kappa_f(1+q_{\kappa}\gamma)} \tag{6}$$

$$\phi_{h}(\gamma) = \frac{\gamma(h_f(1+q_{h}) - h_s) + h_s}{h_f(1+q_{h}\gamma)} \tag{7}$$

where κ_s is the solid thermal conductivity, h_s is the heat transfer coefficient in the solid domain, and q_h and q_κ are interpolation convexity parameters. These interpolation functions enable efficient heat transfer calculations in the 2D simplified model by modifying the governing equations in the solid and fluid domains depending on the γ value. In the bottom layer, where conduction dominates, the governing equation is:

$$\nabla \cdot (\kappa_{s} \nabla T_{bot}) = -\frac{q^{"}}{dz_{base}} + \frac{h_{f} \phi_{h}(\gamma)(T_{bot} - T_{top})}{dz_{base}} \tag{8}$$

where dz_{base} is the thickness of the heat sink base, and $q^{''}$ is the extracted heat flux at the bottom layer. For heat sinks attached to the cold side of TEGs, the extracted heat rate Q_{sink} can be approximated using a 1D heat conduction assumption [34]:

$$\int q^{"} dA = Q_{sink} \approx IST_{sink} + \frac{1}{2} I^{2} R + K(T_{source} - T_{sink}) \tag{9}$$

$$T_{sink} \approx T_{bot} \tag{10}$$

where I is the electrical current flowing through the TEG, S is the device Seebeck coefficient, R is resistance, K is thermal conductance, T_{source} and T_{sink} are the heat source and heat sink side temperatures of the TEG, respectively, and A is the cold side surface area of the TEG. In potential applications for TEGs, including waste heat recovery, the heat source typically has a significantly larger thermal mass than the TEG itself. As a result, the heat source can be assumed to maintain a constant temperature [2]. Under this condition, T_{sink}, and consequently the extracted heat flux $q^{''}$, is influenced by heat sink performance. As fin shapes change during iterations in topology optimization, heat sink performance also changes, altering $q^{''}$. Conventional topology optimization models for heat sinks often do not account for these variations as $q^{''}$ is typically set as a constant in boundary conditions [19,23,33,35].

To address this issue, as shown below in Fig. 2, we modified the topology optimization model by integrating a 3D TEG module to numerically calculate the changing $q^{''}$ during optimization process. This integration accounts for both the TE properties and geometric structure of the TEG, which influence $q^{''}$. The energy generated by the TEG was calculated by creating a closed circuit with an external resistive load. The output power of the TEG corresponds to the power consumed by the resistive load, and the external load resistance was matched to the R of the TEG, since the output power is maximized under this condition [36].

The computational cost of the topology optimization model was further reduced by leveraging the geometric periodicity of the TEG. Since the n-type and p-type TE legs in conventional TEGs are connected in series and share the same geometric shape, we applied symmetry boundary conditions, reducing the computational domain to a single geometric period as shown in Fig. 1b. This resulted in a TO model with reduced computational cost, making it well-suited for optimizing heat sinks in TE generation applications.

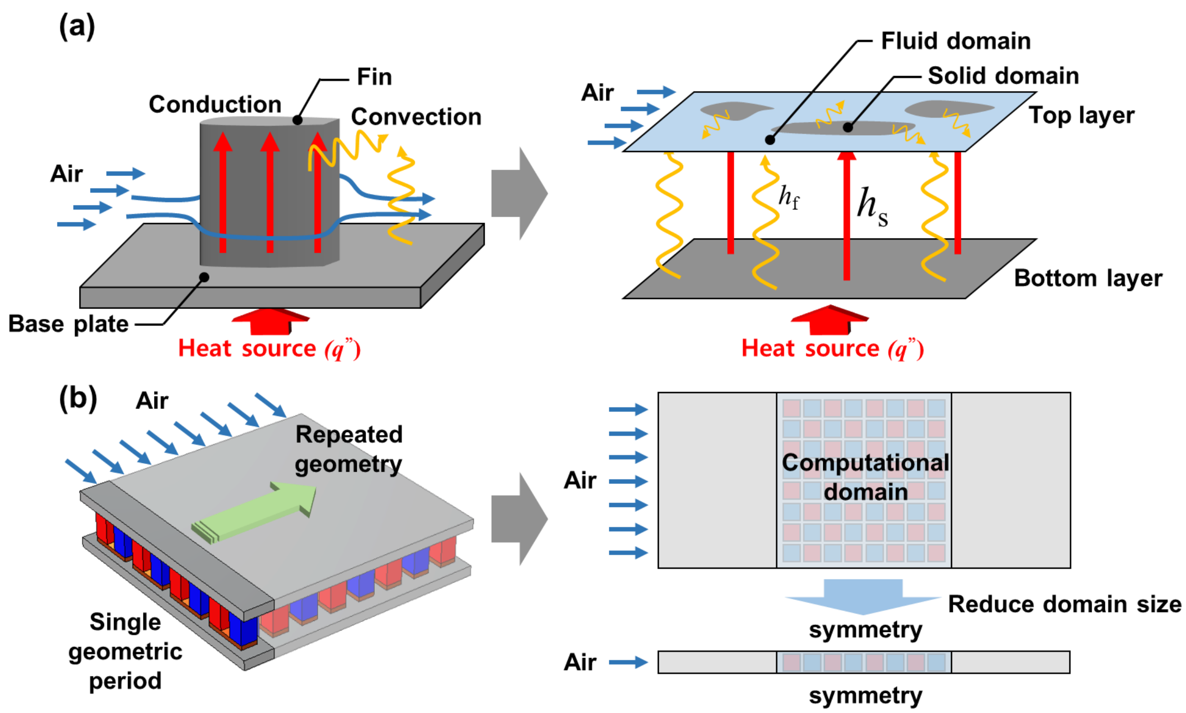

Figure 1. (a) Simplified 2D two-layer topology optimization model for heat transfer simulation. (b) Domain size reduction by leveraging the geometric periodicity of a thermoelectric generator (TEG).

2.2. Optimization model construction

The topology optimization model was constructed using a COMSOL Multiphysics 6.2 as shown in Fig. 2. Materials properties and constant parameter values were determined to numerically solve the governing equations. AlSi10Mg was selected as the fin material due to its compatibility with additive manufacturing through the laser powder bed fusion method and its high thermal conductivity of 130 W/mK at room temperature, making it suitable for a heat sink [37]. The fin height dz_{fin} and base height dz_{base} were set to 7 mm and 2 mm, respectively. The heat transfer coefficients, h_{s} and h_{f}, were determined by the geometry and material properties of the heat sink and are listed in Table 1 [23,33].

The TE properties and geometry of the TEG module in the topology optimization model were based on a commercial TEG (ETX4-3-F1-2020-TA-RT-W6, Laird Thermal Systems). The TE properties of the commercial TEG were derived from its performance curve, provided by the manufacturer [38]. The cooling performance curve at 85 °C was fitted to a quadratic function, as the cooling rate Q_{cool} of the TE device is described by:

$$Q_{\mathrm{cool}} = IST_{\mathrm{source}} - \frac{1}{2} I^2 R + K(T_{\mathrm{source}} - T_{\mathrm{sink}}) \tag{11}$$

From the coefficients of the fitted quadratic function, S, R, and K were determined to be 0.01331 V/K, 1.14348 Ω, and 0.7766 W/K, respectively. The commercial TEG measured 20 mm × 20 mm × 4.7 mm and consisted of an 8 × 8 array of TE legs (each measuring 1.35 mm × 1.35 mm × 2.4 mm) and two 0.8 mm thick Al_2O_3 substrates. By leveraging the geometric periodicity of the TEG, the computational domain was reduced to 1/8 of the total area, resulting in a domain size of 20 mm × 2.5 mm. The fluid flow inlet and outlet were extended by 10 mm to ensure developed flow and prevent reverse flow issues. The properties of air used in the topology optimization model are listed in Table 1.

Table. 1. Constant parameters used in the topology optimization model

Parameters	Value
κ_s [W/m·K]	130
κ_f [W/m·K]	0.024
ρ_f [kg/m^3]	1.229
c_f [J/kg·K]	1007
h_f [W/m^2·K]	25
h_s [W/m^2·K]	62000
α [s·N/m^4]	10^6

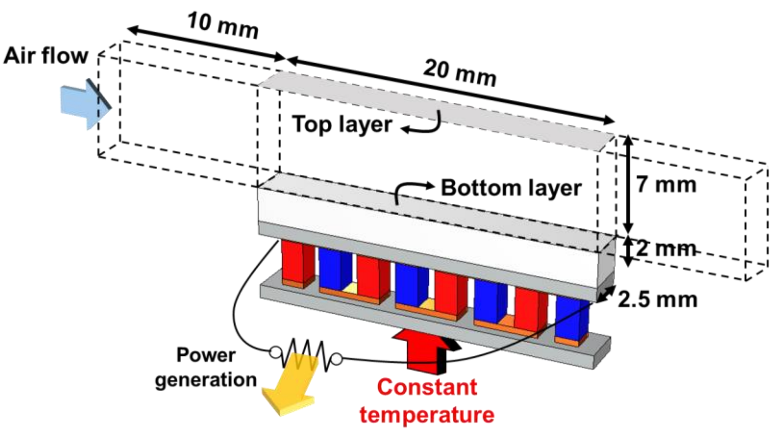

Figure 2. Schematic illustration of the topology optimization model for the heat sink in thermoelectric (TE) generation.

2.3. Optimization problem setup

In this study, a constant T_{source} of 150°C was applied as the boundary condition to simulate a low-grade waste heat recovery scenario, with an ambient temperature of 20°C [2]. When an air-cooled heat sink is attached to the TEG, the conversion efficiency (η) is defined as follows:

$$\eta = \frac{P_{net}}{Q_{source}} = \frac{P_{TE} - P_{pump}}{Q_{source}} \tag{12}$$

$$P_{pump} = \dot{V} \Delta p \tag{13}$$

, where P_{net} is net output power, Q_{source} is the applied heat by the heat source, P_{TE} is output power generated by the TEG, P_{pump} is the power consumed by the pump, $\dot{V}$ is the volumetric flow rate of air, and Δp is the pressure drop between inlet and outlet of the heat sink. According to the equation, η is a multiphysics parameter related to fluid flow, electric potential, and heat transfer. To simplify the optimization by decoupling these multiphysics aspects, the objective was set to maximize P_{TE} rather than directly maximizing η. To prevent the optimized heat sink from resulting in excessive P_{pump}, a constraint was applied to keep Δp below 12 Pa, which is a practical Δp range used for forced convection air-cooled heat sinks [39]:

$$\begin{aligned} &\text{maximize } P_{\mathrm{TE}} \\ &\text{subject to } \Delta p < 12 \text{ Pa} \end{aligned} \tag{14}$$

In Equation (12), under the assumption of 1D heat conduction, ratio between P_{TE} and Q_{source} can be expressed as:

$$\frac{P_{\mathrm{TE}}}{Q_{\mathrm{source}}} \approx \frac{T_{\mathrm{source}} - T_{\mathrm{sink}}}{T_{\mathrm{source}}} \frac{\sqrt{1+ZT} - 1}{\sqrt{1+ZT} + \dfrac{T_{\mathrm{sink}}}{T_{\mathrm{source}}}} \tag{15}$$

, where ZT (= S / KR) is a device thermoelectric figure of merit [40]. From Equations (12) and (15), η increases as the temperature difference (T_{source} - T_{sink}) increases. Therefore, with the constant heat source temperature T_{source} of 150°C, improving the fin structure to decrease T_{sink} leads to increased η. Thus, another optimization problem was solved to minimize T_{sink} under the same Δp constraint used in Eq. (14):

$$\begin{aligned} &\text{minimize } T_{\mathrm{sink}} \\ &\text{subject to } \Delta p < 12 \text{ Pa} \end{aligned} \tag{16}$$

When solving Eqs. (14) and (16) using topology optimization, a Helmholtz-type density filter was applied to prevent the checker board problem and control the minimum size of the fin shape [41]:

$$-r^2 \nabla^2 \tilde{\gamma} + \tilde{\gamma} = \gamma \tag{17}$$

where r controls the minimum fin size and $\tilde{\gamma}$ is the filtered design variable. After applying the density filter, $\tilde{\gamma}$ replaces γ in all governing equations. Subsequently, topology optimization was conducted following the process shown in Fig. 3. In this process, the convexity parameters were gradually changed every 100 iterations to apply stronger penalization. The values of convexity parameters are listed in Table 2.

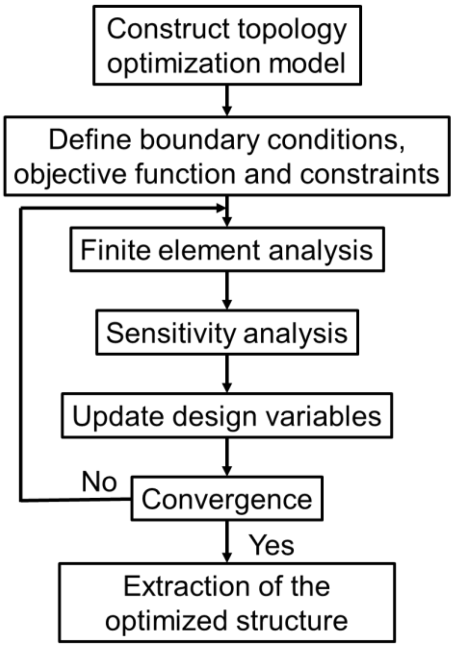

Figure 3. Diagram of multi-stage topology optimization process

Table 2. Convexity parameters used in the topology optimization model

Parameters	Value
q_α	{500, 100, 10}
q_κ	{10, 50, 100}
q_h	{10, 50, 100}

2.4 Topology optimization results

The optimization results are shown in Fig. 4. Two TO heat sinks were obtained by solving the optimization problems in Eqs. (14) and (16). A threshold value of 0.5 was applied to the resulting γ field: regions with γ lower than 0.5 were identified as solid fins, while regions with

γ higher than 0.5 were considered fluid domains. Using this extracted fin structure, a 3D heat sink model was created by extruding the fins to a height of 7 mm with a 2 mm thick base plate. The two optimization results showed negligible differences in their topology, confirming that the primary mechanism for enhancing P_{TE} is the reduction of T_{sink}. This highlights the importance of using a heat sink with low thermal resistance to achieve high P_{TE} in a TEG. Since the geometries of the two TO heat sinks were nearly identical, further discussion will focus on the TO heat sink optimized for maximizing P_{TE} (Fig. 4a).

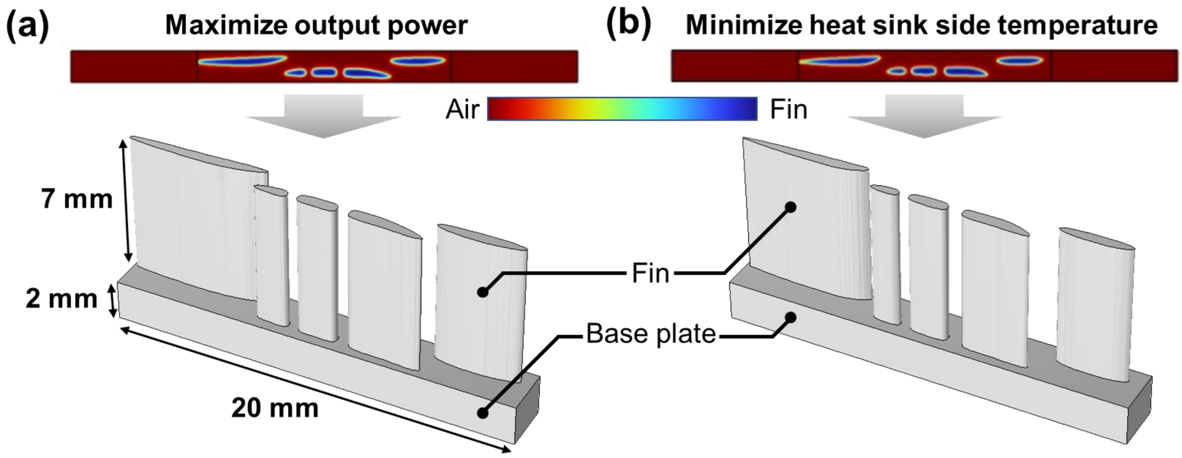

Figure 4. Topology optimization results and 3D models of the optimized fin structures obtained by solving the optimization problems: (a) maximizing output power (P_{TE}), and (b) minimizing the heat sink side temperature of the TEG (T_{sink}).

3. Numerical simulation and experimental setups

3.1. Numerical simulation setup

The numerical simulation was performed using a 3D heat sink model under the same boundary conditions as the topology optimization model. The heat source temperature was set to 150°C, and a 3D TEG model with identical properties and geometry to the topology optimization model was attached. The material properties of other components, including the heat sink and air, were set to match those in the topology optimization model. The performance of the heat sink was evaluated under flow conditions with a Δp ranging from 6 Pa to 30 Pa, with extended inlet and outlet sections of 10 mm each, assuming incompressible flow at steady state. The simulation was conducted using the COMSOL Multiphysics 6.2.

A mesh dependency study was performed at the optimization condition of 12 Pa. The mesh density was gradually increased until the inlet air velocity, T_{sink}, and P_{TE} showed deviations of less than 1% with further refinement, as shown in Table 3. Based on this study, the final mesh was set to approximately 4.8 million elements. To evaluate the performance of the TO heat sink by comparison, a conventional rectangular-fin heat sink was also modeled and simulated under the same boundary conditions. The conventional heat sink featured six rectangular fins, each measuring 1 mm × 2.3 mm with a 1.24 mm spacing.

Table 3. Mesh refinement study results

Number of Mesh elements	Air velocity [m/s]	T_{sink} [°C]	P_{TE} [W]
3157220	2.312	343.80	0.0275
4321865	2.341	343.82	0.0275
4848890 (selected)	2.361	343.82	0.0275

3.2 Experimental setup

The experimental validation was conducted using the same fin geometry as the numerical simulations for both the TO heat sink and the conventional heat sink. To match the size with the commercial TEG, the reduced domain size (used in the simulation through geometric periodicity) was restored to full size using mirror symmetry, as shown in Fig. 5a and b. As a result, 3D models of the conventional and TO heat sinks, each with the full dimensions of 20 mm × 20 mm × 7 mm, were obtained and fabricated using laser powder bed fusion with AlSi10Mg, as shown in Fig. 5c. The additive manufacturing method was selected due to its suitability for producing the non-intuitive TO structure.

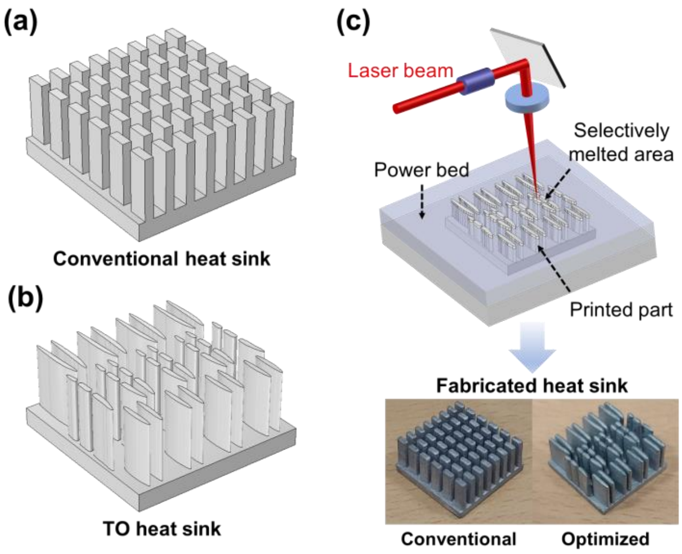

Figure 5. 3D models of (a) conventional heat sink with rectangular fins and (b) topology optimized (TO) heat sink. (c) Schematic of the heat sink fabrication process using laser powder bed fusion.

The performance of both the conventional and TO heat sinks was experimentally evaluated using a wind tunnel experiment as shown in Fig. 6a. A 6-ohm resistive heater was attached to a high thermal conductivity BeO plate heat spreader (275 W/mK, MTI Instruments Inc.), which was then mounted on one side of a commercial TEG (ETX4-3-F1-2020-TA-RT-W6, Laird Thermal Systems) using thermal grease (H grease, Apiezon) to minimize thermal contact resistance. The TO or conventional heat sink was attached to the other side of the TEG using thermal grease. Two T-type thermocouples were placed on the heater-attached side (hot side) and the heat sink-attached side (cold side) of the TEG. Subsequently, the assembled TEG module was inserted into a Teflon insulating block with a low thermal conductivity (0.2 W/mK) to minimize parasitic heat loss, as shown in Fig. 6b. The TEG module, enclosed by the Teflon block was positioned at the test section of the wind tunnel (Fig. 6a). The hot side temperature was maintained at 150°C by adjusting the heat supplied by the heater.

For the wind tunnel experiment, a 500 mm-long rectangular duct with a flow straightener at the inlet, featuring a 7 mm × 20 mm cross-sectional area, was placed before the test section to ensure fully developed laminar flow. Another 250 mm-long rectangular duct was placed after the test section, with a blower (CBM-5015BF-055-391-20, Same Sky) installed at the end of the duct to create air flow from the inlet to the outlet. The ambient temperature was maintained at 20°C using an air conditioning unit to match the topology optimization boundary conditions. A T-type thermocouple was used to measure the inlet air temperature outside the test section. The Δp across the test section was measured by a differential pressure transducer and varied from 6 Pa to 30 Pa by the blower. The maximum inlet flow velocity (V_{max}) was measured by a pitot tube located before the test section. Another differential pressure transducer measured the difference between total pressure (p_{t}) and static pressure (p_{s}) in the pitot tube to calculate V_{max} as follows:

$$V_{\mathrm{max}} = \sqrt{\frac{2(p_{\mathrm{t}} - p_{\mathrm{s}})}{\rho_{\mathrm{f}}}} \tag{18}$$

The calculated V_{max} was then converted into an average flow velocity (V_{avg}) using the following relation [42]:

$$V_{\mathrm{avg}} = 0.25 V_{\mathrm{max}} \left(\frac{\Gamma(1/2)\Gamma(1+1/n)}{\Gamma(3/2+1/n)} \right)^2 \tag{19}$$

, where Γ is a gamma function, and n was taken as 7 as suggested by [42].

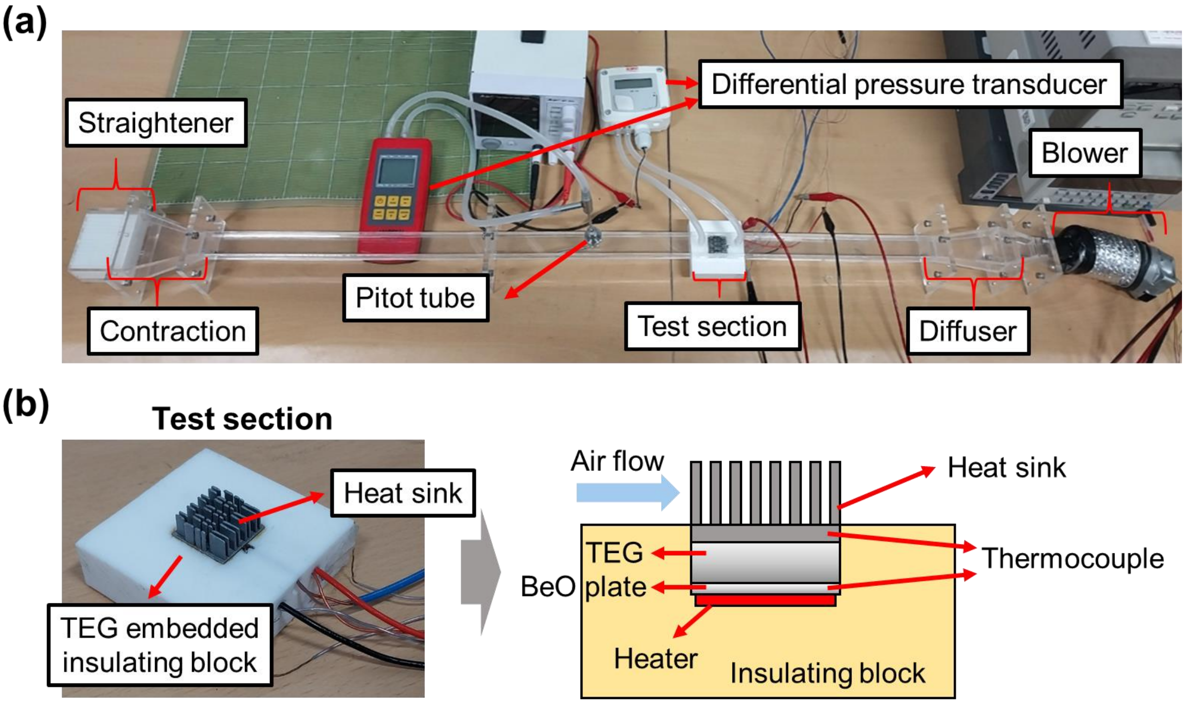

Figure 6. (a) Image and schematic illustration of the test section. (b) Image of the wind tunnel experimental setup.

4. Results and discussion

4.1 Fluid flow and heat transfer characteristics of topology optimized heat sink

The V_{avg} for both the conventional and TO heat sinks was derived from Eq. (19), over Δp range from 6 Pa to 30 Pa, as shown in Fig. 7a. For both heat sinks, the simulation results closely match the experimental data, confirming that the additive manufacturing successfully produced the fin geometries. The slightly higher deviation between the simulation and experiment for the TO heat sink, compared to the conventional heat sink, is likely due to the non-intuitive shape of the heat sink, which may introduce minor discrepancies between the simulation model and the fabricated heat sink. At the same Δp, the inlet V_{avg} of the TO heat sink is approximately 40% higher than that of the conventional heat sink, leading to a corresponding ~40% increase in P_{pump}, as shown in Fig. 7b.

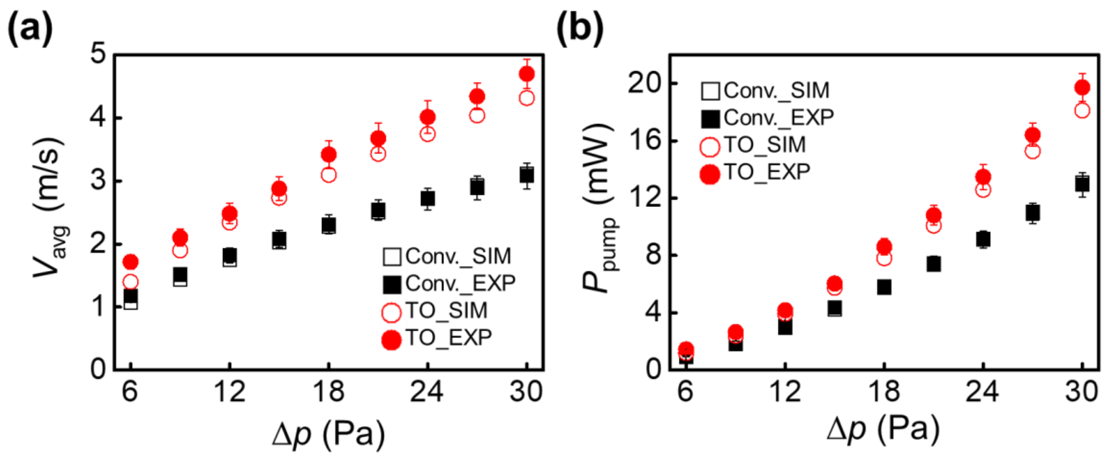

Figure 7. (a) Experimental (EXP) and simulated (SIM) result of inlet air velocity (V_{avg})and (b) power consumption (P_{pump}) of conventional (Conv.) and TO heat sink as a function of pressure drop across heat sink (Δp).

The performance of the heat sinks can be compared by evaluating their thermal resistances (R_{th}). R_{th} of a heat sink is calculated using the equation:

$$R_{th} = \frac{T_{sink} - T_{amb}}{Q_{sink}} \tag{20}$$

, where T_{amb} is the ambient temperature. In the case of a closed-circuited TEG, the generated electrical current induces the Peltier effect, making it difficult to accurately evaluate Q_{sink} (Eq. (9)). To accurately determine Q_{sink} without the influence of the Peltier effect, R_{th} was measured with the short-circuited TEG. Under this condition, $Q_{sink} = Q_{source}$, assuming negligible heat loss from the TEG to the insulating block. While Q_{source} can be derived from the experimental heat rate value applied by the heater, parasitic heat loss through the insulating block must be taken into account for reliable estimation of Q_{source}. To address this issue, the parasitic heat loss was approximated by measuring the bottom-side temperature of the insulating block. When the heat source was maintained at 150°C, the temperature at the center of the bottom side of the insulating block was consistently measured at 60°C. The parasitic heat loss through the insulating block was determined to be 2.6 W, by numerically simulating the temperature distribution of the insulating block under the aforementioned temperature conditions using the COMSOL Multiphysics 6.2. As a result, Q_{source} in the experiment was determined by subtracting 2.6 W from the heat rate applied by the heater. With varying Δp, Q_{source} from the experiment closely matches the Q_{source} calculated by the numerical simulation (Fig. 8a), wherein $Q_{\text{sink}} = Q_{\text{source}}$. This result indicates that the proposed method can successfully obtain reasonably accurate Q_{source} (and thus Q_{sink}) values.

As shown in Fig. 8b, T_{sink} decreases by approximately 13 K when the TO heat sink is attached compared to the conventional heat sink. Due to the decrease of T_{sink}, the TO heat sink shows lower R_{th} compared to the conventional heat sink at the same Δp, specifically 33.5% lower R_{th} at 12 Pa (Fig. 8c), which corresponds to the upper limit of Δp used for topology optimization as given in Eqs. (14) and (16). This indicates that the fin structure of the TO heat sink was successfully optimized to reduce R_{th}. Although the TO heat sink consumes more P_{pump} than the conventional heat sink, the significant reduction in R_{th} allows the TO heat sink to achieve a lower R_{th} than the conventional heat sink at the same P_{pump}, as shown in Fig. 8d.

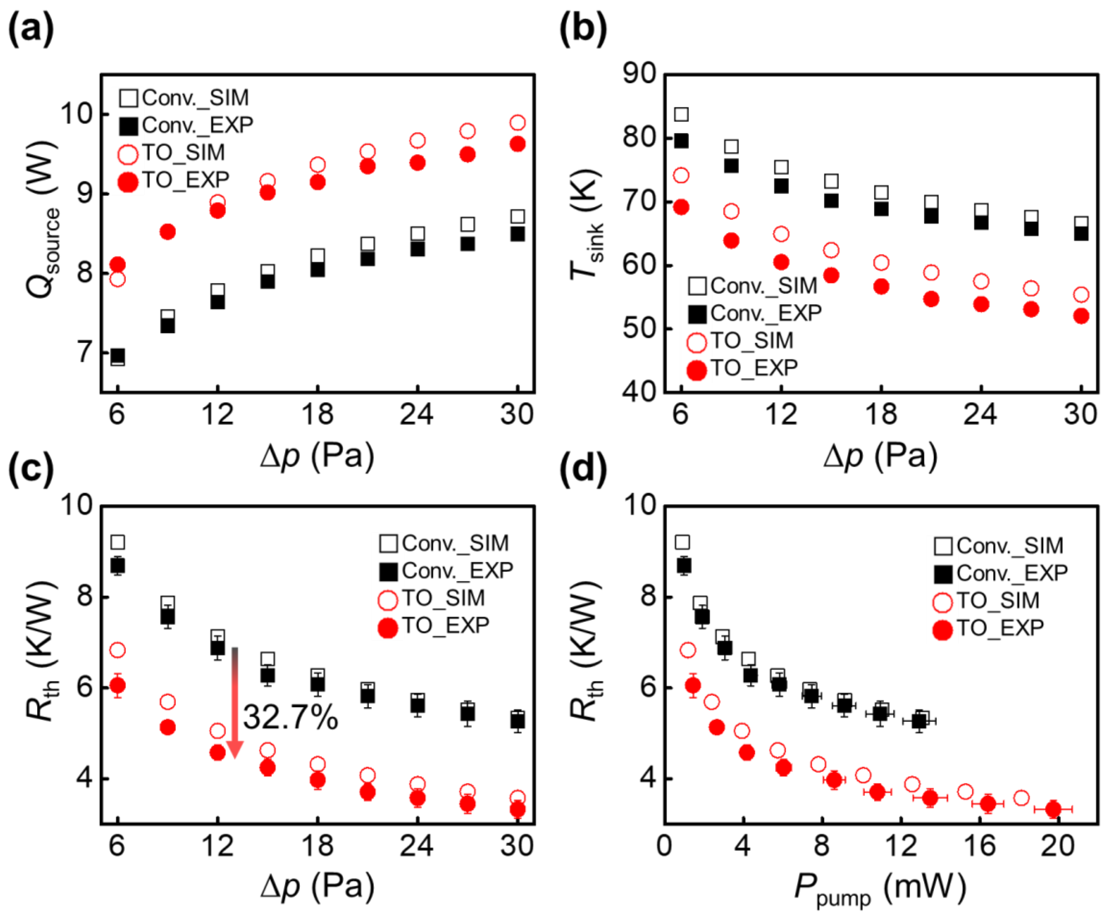

Figure 8. Experimental and simulated results for (a) heat applied from heat source (Q_{source}), (b) heat sink side temperature of the TEG (T_{sink}), and (c) thermal resistance (R_{th}) of the heat sinks as a function of Δp. (d) R_{th} of the heat sinks as a function of P_{pump}.

4.2 Performance of commercial thermoelectric generator with topology optimized heat sink

P_{TE} was measured by performing I-V curve analysis on the closed-circuited TEG. The voltage across TEG was measured while applying electrical current from 0 mA up to the optimal current that maximizes P_{TE}. The P_{TE} was calculated by multiplying the measured voltage by the applied current. Due to the reduced R_{th}, the TO heat sink induces a larger temperature difference across the TEG compared to the conventional heat sink. This increased temperature difference resulted in higher P_{TE} for Δp of 6 Pa to 30 Pa, specifically 44.7% increased P_{TE} at 12 Pa (Fig. 9a). This significant improvement in P_{TE} leads to a 21.3% increase in η at 12 Pa from 1.78 % to 2.16 %, as shown in Fig. 9b, despite the TO heat sink consuming 40% more P_{pump}.

Assuming the same temperature difference across the TEG (T_{source} - T_{sink}) for both cases of the conventional and TO heat sinks, η can be converted into ZT of the TEGs using Eq. (15) over the Δp range of 6 Pa to 30 Pa (Fig. 9c). This approach translates the difference in η between the two heat sink cases, where ZT of the TEGs are the same, into the difference in ZT between the two TEGs, where use of the same heat sink (thus the same T_{source} - T_{sink}) is assumed. We label such a ZT estimated under the same T_{source} - T_{sink} assumption as the effective ZT for the following discussion. At 12 Pa, the effective ZT of the TEG is 0.49 with the conventional heat sink, while the effective ZT with the TO heat sink is 0.62, representing a 27% improvement. Therefore, 21.3% improvement in η at Δp of 12 Pa is equivalent to a 27% increase in the ZT of the TEG without modifying the heat sink. The 27% improved ZT corresponds to a highly challenging achievement, as it would typically require the discovery of novel TE materials with high figure of merits, which is both time-consuming and costly. It is remarkable that the equivalent improvement was simply achieved in this study by optimizing the fin structure through topology optimization. Furthermore, despite the higher P_{pump} of the TO heat sink, it still showed much higher P_{TE}, η, and effective ZT compared to the conventional heat sink when evaluated at the same P_{pump}, as shown in Figs. 9d-f. This highlights the effectiveness of TO heat sink in achieving superior P_{TE} and η in TE power generation.

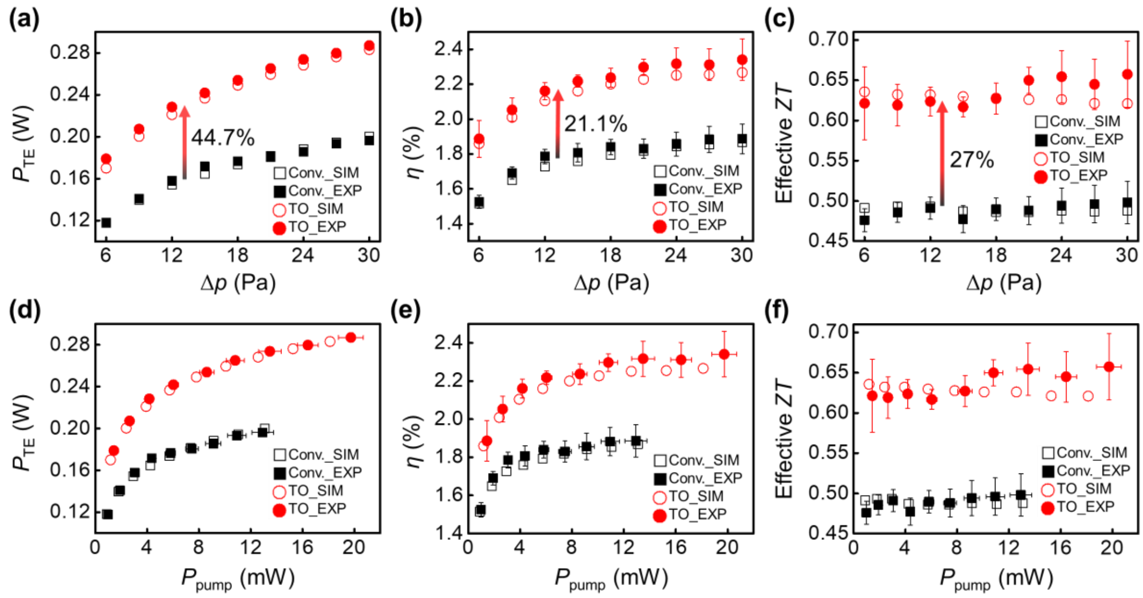

Figure 9. Experimental and simulated results of (a) output power (P_{TE}), (b) conversion efficiency (η), and (c) effective device thermoelectric figure of merit (effective ZT) of a commercial TEG as a function of Δp. Experimental and simulated results of (d) P_{TE}, (e) η, and (f) effective ZT of a commercial TEG as a function of P_{pump}. Effective ZT values in (c) and (f) were estimated by assuming the same temperature difference across the TEG (T_{source} - T_{sink}) for both cases of the conventional and TO heat sinks.

4.3 Temperature uniformity of topology optimized heat sink

In air-cooled heat sinks, as heat is transferred from the heat sink to the airflow, the air temperature gradually rises along the airflow direction. This results in an increase in the T_{sink} along the airflow direction, creating a non-uniform temperature distribution [43]. In TE power generation, this non-uniform temperature distribution reduces the output power of TE leg pairs along the airflow direction, resulting in an overall degradation of P_{TE}. Furthermore, uneven thermal stress is induced, which decreases the durability of TEGs [44,45]. Therefore, both reducing T_{sink} and achieving uniformity in T_{sink} are important for TEGs to achieve high P_{TE} and reliability.

Figure 10a shows the simulation result of the T_{sink} distribution, adjusted by subtracting the minimum value of T_{sink}, at Δp of 12 Pa. In the conventional heat sink, the non-uniformity of T_{sink} leads to a reduction in the P_{TE} of the TE leg pairs, particularly for those positioned farther from the flow inlet, as shown in Fig. 10b. However, with the TO heat sink, this non-uniformity is significantly reduced, preventing the decrease in P_{TE}. Specifically, the difference between the maximum and minimum T_{sink} (ΔT_{sink}) decreases from 3.33 K to 2.12 K, and the degradation of the P_{TE} for the 4th TE leg pair is reduced from 6.4% to 3.8%, compared to the conventional heat sink (Figs. 10a and b).

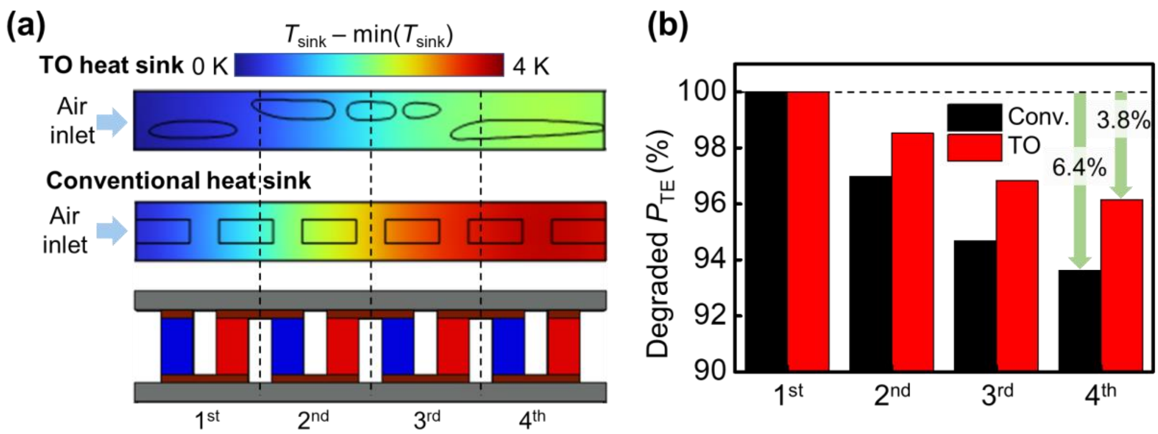

Figure 10. (a) T_{sink} distribution, adjusted by subtracting the minimum value of T_{sink}, at Δp of 12 Pa. (b) The degraded P_{TE} at the nth TE leg pair, calculated by the ratio of the P_{TE} for the nth TE leg pair to the P_{TE} of the 1st TE leg pair.

The improvement of T_{sink} uniformity can be explained by the airflow velocity field and the local heat transfer coefficient (h_{loc}) obtained from numerical simulation results for each heat sink, as shown in Fig. 11 [46]. For both heat sinks, h_{loc} increases at the fin locations where the fins enhance convective heat transfer. In the conventional heat sink, the same shape fins are arranged in a row, so each upstream fin obstructs airflow to the fins behind it (Fig. 11a), resulting in a decrease of h_{loc} along the airflow direction, as shown in Fig. 11b. This reduction of h_{loc} together with the continuous increase of air temperature along the airflow direction leads to a non-uniform T_{sink} distribution.

In contrast, the TO heat sink exhibits a unique trend in h_{loc} due to its non-periodic fin arrangement, allowing airflow to reach downstream fins more effectively, as shown in Fig. 11a. Specifically, due to the optimized airflow, h_{loc} for the fin located near the flow outlet still maintains a high value, as shown in Fig. 11b. This high h_{loc} compensates the rising air temperature and thereby reduces the T_{sink} non-uniformity. Moreover, the TO heat sink achieves an overall increase in h_{loc} with lower variation along the airflow direction compared to the conventional heat sink. Specifically, the standard deviation of h_{loc} decreases from 469 W/m^{2}K to 398 W/m^{2}K, while the average h_{loc} increases from 639 W/m^{2}K to 878 W/m^{2}K for the TO heat sink, compared to the conventional heat sink. Therefore, the improved T_{sink} uniformity in the TO heat sink can be understood as a result of favorable airflow dynamics and heat transfer characteristics across the heat sink due to the non-periodic fin arrangement, leading to an enhanced P_{TE} of the TEG compared to when the conventional heat sink is used.

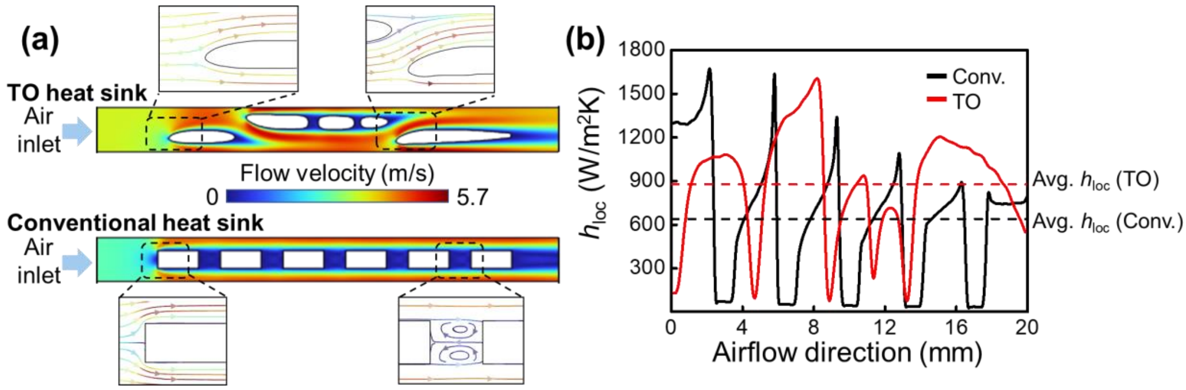

Figure 11. (a) Airflow velocity field (insets are the streamlines) and (b) local heat transfer coefficient (h_{loc}) of the conventional (Conv.) and TO heat sinks at Δp of 12 Pa.

We studied the relationship between Δp and T_{sink} uniformity, as the improved T_{sink} uniformity observed in the TO heat sink is attributed to its favorable airflow dynamics which is expected to be influenced by Δp. Figures 12a and b show h_{loc} of each heat sink, evaluated from the numerical simulation results with increasing Δp. As Δp increases, the overall h_{loc} along the airflow direction increases for both heat sinks. In the conventional heat sink, the most significant increase in h_{loc} occurs at the first fin, while the subsequent fins experience only slight increases with Δp due to airflow obstruction caused by the upstream fins, which diminishes the sensitivity of h_{loc} to the airflow dynamics or Δp. Such an airflow obstruction also intensifies the decreasing trend of h_{loc} along the airflow direction. Conversely, in the TO heat sink, a significant increase in h_{loc} occurs across all fins, with the fin at the flow outlet experiencing a similar level of h_{loc} increase as the fin at the inlet, due to the absence of obstruction by the upstream fins. As a result, ΔT_{sink} shows an opposite dependency on Δp for each heat sink, as shown in Fig. 12c. In the conventional heat sink, ΔT_{sink} increases with higher Δp, suggestive of intensifying T_{sink} non-uniformity, whereas in the TO heat sink, the opposite is observed. The negative correlation between ΔT_{sink} and Δp in the TO heat sink is advantageous for scaling up TEGs, in which both ΔT_{sink} and Δp increase due to longer airflow paths. In such a case, the increased Δp effectively compensate the increase in ΔT_{sink}, allowing the scaled-up TEGs to maintain their power generation performances.

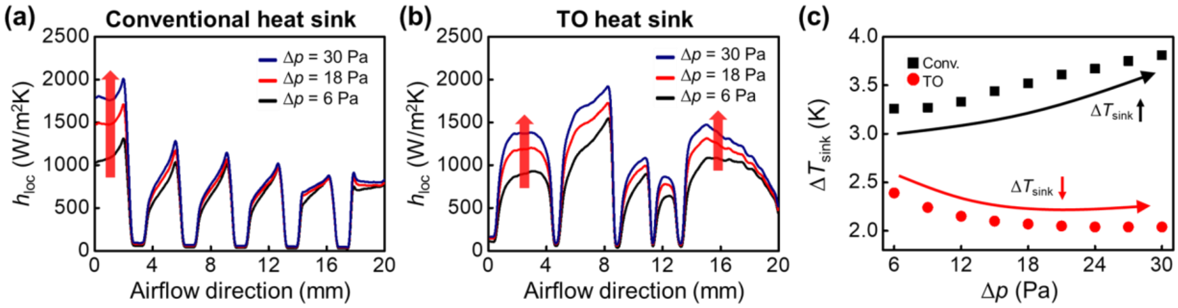

Figure 12. h_{loc} for (a) the conventional and (b) TO heat sink under Δp ranging from 6 to 30 Pa. (c) Difference between the maximum and minimum T_{sink} (ΔT_{sink}) of the conventional and TO heat sink under Δp ranging from 6 to 30 Pa.

5. Conclusions

This study demonstrated the effectiveness of topology optimization for designing a high-performance air-cooled heat sink for TEGs. A simplified 2D two-layer topology optimization model was combined with a 3D TEG module to reduce the computational cost, while considering the geometric structure and TE properties of TEGs. This model solved two optimization problems: maximizing P_{TE} and minimizing T_{sink}, and resulted in two TO heat sinks with almost identical fin geometries.

One TO heat sink was then fabricated using additive manufacturing, and its performance was experimentally validated. Compared to a conventional rectangular-fin heat sink, the TO heat sink demonstrated a significant reduction in R_{th} and an increase in P_{TE} across a wide range of Δp (6 Pa to 30 Pa). Specifically, at 12 Pa, R_{th} was reduced by 33.5%, therefore, the P_{TE} of the commercial TEG was improved by 44.7%. Although the TO heat sink consumes 40% more P_{pump}, the substantial increase in P_{TE} outweighs this larger power input, resulting in a 21.3% improvement in η compared to the case where the conventional heat sink is used. This improvement in η is equivalent to a 27% increase in the ZT of the TEG, achieved solely and simply by adopting TO heat sinks without the need to develop novel TE materials, which is time-consuming and costly.

Numerical simulations revealed that the non-periodic geometry of the TO heat sink improves the uniformity of T_{sink} distribution, which is crucial for practical applications as it enhances P_{TE} and thermal stability of TEGs [44,45]. The improvement in T_{sink} uniformity with the TO heat sink became more pronounced with higher Δp, underscoring the potential importance of the TO heat sink in scaled-up TEG systems with longer airflow paths and higher Δp.

While our study successfully showed that TO heat sinks can significantly enhance the power generation performance of a commercially-available TEG with a standard geometry, there is a growing interest in diversifying TEG geometry by altering the leg shape [47], spacing [48], dimensions [49], etc. Since the varying TEG geometries impose different boundary conditions for topology optimization, one interesting research direction would be to investigate TO heat sinks for such diverse TEG geometries.

Credit authorship contribution statement

Junyoung Park: Conceptualization, Data curation, Formal analysis, Investigation, Methodology, Validation, Writing - Original Draft, Writing - Review & Editing. **Hyun Yu:** Formal analysis, Methodology, Validation, Writing - Review & Editing. **Ki Mun Bang:** Methodology, Validation. **Woochul Kim:** Methodology, Validation. **Hyungyu Jin:** Conceptualization, Funding acquisition, Project administration, Resources, Supervision, Writing - Review & Editing.

Declaration of Competing Interest

The authors declare that they have no known competing financial interests or personal relationships that could have appeared to influence the work reported in this paper.

Acknowledgments:

The authors thank Seokyeong Byeon for valuable discussions and insights during the preparation of the manuscript. This work was supported by the National Research Foundation of Korea (NRF) grants funded by the Korea government (MSIT) (NRF-2022M3C1A3091988, RS-2024-00449743, and RS-2024-00345022).

References

[1] A.G. Olabi, M.A. Abdelkareem, Renewable energy and climate change, Renew Sustain Energy Rev 158 (2022) 112111, https://doi.org/10.1016/j.rser.2022.112111.

[2] W.H. Chen, M. Carrera Uribe, E.E. Kwon, K.Y.A. Lin, Y.K. Park, L. Ding, et al., A comprehensive review of thermoelectric generation optimization by statistical approach: Taguchi method, analysis of variance (ANOVA), and response surface methodology (RSM), Renew Sustain Energy Rev 169 (2022) 112917, https://doi.org/10.1016/j.rser.2022.112917.

[3] D. Champier, Thermoelectric generators: A review of applications, Energy Convers Manag 140 (2017) 167–181, https://doi.org/10.1016/j.enconman.2017.02.070.

[4] A. Nozariasbmarz, F. Suarez, J.H. Dycus, M.J. Cabral, J.M. LeBeau, M.C. Öztürk, et al., Thermoelectric generators for wearable body heat harvesting: Material and device concurrent optimization, Nano Energy 67 (2020) 104265, https://doi.org/10.1016/j.nanoen.2019.104265.

[5] W. Li, A. Nozariasbmarz, R.A. Kishore, H.B. Kang, C. Dettor, H. Zhu, et al., Conformal High-Power-Density Half-Heusler Thermoelectric Modules: A Pathway toward Practical Power Generators, ACS Appl Mater Interfaces 13 (2021) 53935–53944, https://doi.org/10.1021/acsami.1c16117.

[6] B. Orr, A. Akbarzadeh, M. Mochizuki, R. Singh, A review of car waste heat recovery systems utilising thermoelectric generators and heat pipes, Appl Therm Eng 101 (2016) 490–495, https://doi.org/10.1016/j.applthermaleng.2015.10.081.

[7] F. Tohidi, S. Ghazanfari Holagh, A. Chitsaz, Thermoelectric Generators: A comprehensive review of characteristics and applications, Appl Therm Eng 201 (2022) 117793, https://doi.org/10.1016/j.applthermaleng.2021.117793.

[8] R. Kiflemariam, C.X. Lin, Experimental investigation on heat driven self-cooling application based on thermoelectric system, Int J Therm Sci 109 (2016) 309–322. https://doi.org/10.1016/j.ijthermalsci.2016.06.001.

[9] M.R. Gomaa, H. Rezk, Passive cooling system for enhancement the energy conversion efficiency of thermo-electric generator, Energy Rep 6 (2020) 687–692, https://doi.org/10.1016/j.egyr.2020.11.149.

[10] R.A. Kishore, A. Nozariasbmarz, B. Poudel, M. Sanghadasa, S. Priya, Ultra-high performance wearable thermoelectric coolers with less materials, Nat Commun 10 (2019) 1765, https://doi.org/10.1038/s41467-019-09707-8.

[11] H.H. Wu, Y.Y. Hsiao, H.S. Huang, P.H. Tang, S.L. Chen, A practical plate-fin heat sink model, Appl Therm Eng 31.5 (2011) 984–992, https://doi.org/10.1016/j.applthermaleng.2010.10.014.

[12] W.H. Chen, M. Carrera Uribe, D. Luo, L. Jin, L. Huat Saw, R. Lamba, Taguchi optimization and analysis of variance for thermoelectric generators with forced convection air cooling, Appl Therm Eng 231 (2023) 120878, https://doi.org/10.1016/j.applthermaleng.2023.120878.

[13] S. Lv, W. He, Q. Jiang, Z. Hu, X. Liu, H. Chen, M. Liu, Study of different heat exchange technologies influence on the performance of thermoelectric generators, Energy Convers Manag 156 (2018) 167–177, https://doi.org/10.1016/j.enconman.2017.11.011.

[14] C.C. Wang, C.I. Hung, W.H. Chen, Design of heat sink for improving the performance of thermoelectric generator using two-stage optimization, Energy 39 (2012) 236–245, https://doi.org/10.1016/j.energy.2012.01.025.

[15] J. Kim, S. Khan, P. Wu, S. Park, H. Park, C. Yu, W. Kim, Self-charging wearables for continuous health monitoring, Nano Energy 79 (2021) 105419, https://doi.org/10.1016/j.nanoen.2020.105419.

[16] M. Lossec, B. Multon, H. Ben Ahmed, Sizing optimization of a thermoelectric generator set with heatsink for harvesting human body heat, Energy Convers Manag 68 (2013) 260–265, https://doi.org/10.1016/j.enconman.2013.01.021.

[17] T. Pujol, I. T'Jollyn, E. Massaguer, A. Massaguer, I.R. Cózar, M. De Paepe, Design optimization of plate-fin heat sink with forced convection for single-module thermoelectric generator, Appl Therm Eng 221 (2023) 119866, https://doi.org/10.1016/j.applthermaleng.2022.119866.

[18] A.A. Koga, E.C.C. Lopes, H.F. Villa Nova, C.R.D. Lima, E.C.N. Silva, Development of heat sink device by using topology optimization, Int J Heat Mass Transf 64 (2013) 759–772. https://doi.org/10.1016/j.ijheatmasstransfer.2013.05.007.

[19] G. Lee, I. Lee, S.J. Kim, Topology optimization of a heat sink with an axially uniform cross-section cooled by forced convection, Int J Heat Mass Transf 168 (2021) 120732, https://doi.org/10.1016/j.ijheatmasstransfer.2020.120732.

[20] F. Chen, J. Wang, X. Yang, Topology optimization design and numerical analysis on cold plates for lithium-ion battery thermal management, Int J Heat Mass Transf 183 (2022) 122087, https://doi.org/10.1016/j.ijheatmasstransfer.2021.122087.

[21] T. Borrvall, J. Petersson, Topology optimization of fluids in Stokes flow, Int J Numer Methods Fluids 41 (2003) 77–107, https://doi.org/10.1002/fld.426.

[22] J. Alexandersen, O. Sigmund, N. Aage, Large scale three-dimensional topology optimisation of heat sinks cooled by natural convection, Int J Heat Mass Transf 100 (2016) 876–891, https://doi.org/10.1016/j.ijheatmasstransfer.2016.05.013.

[23] S. Zeng, B. Kanargi, P.S. Lee, Experimental and numerical investigation of a mini channel forced air heat sink designed by topology optimization, Int J Heat Mass Transf 121 (2018) 663–679, https://doi.org/10.1016/j.ijheatmasstransfer.2018.01.039.

[24] J. Ning, X. Wang, H. Huang, S. Wang, W. Yan, Topology optimized novel additively manufactured heat sink: experiments and numerical simulations, Energy Convers Manag 286 (2023) 117024, https://doi.org/10.1016/j.enconman.2023.117024.

[25] J. Palumbo, O. Tayyara, C.H. Amon, S. Chandra, Topologically optimized mini-channel heat sinks for reduced temperature non-uniformity, Int J Heat Mass Transf 214 (2023) 124421, https://doi.org/10.1016/j.ijheatmasstransfer.2023.124421.

[26] H. Li, X. Ding, F. Meng, D. Jing, M. Xiong, Optimal design and thermal modelling for liquid-cooled heat sink based on multi-objective topology optimization: An experimental and numerical study, Int J Heat Mass Transf 144 (2019) 118638, https://doi.org/10.1016/j.ijheatmasstransfer.2019.118638.

[27] D. Martínez-Maradiaga, A. Damonte, A. Manzo, J.H.K. Haertel, K. Engelbrecht, Design and testing of topology optimized heat sinks for a tablet, Int J Heat Mass Transf 142 (2019) 118429, https://doi.org/10.1016/j.ijheatmasstransfer.2019.07.079.

[28] A. Zou, R. Chuan, F. Qian, W. Zhang, Q. Wang, C. Zhao, Topology optimization for a water-cooled heat sink in micro-electronics based on Pareto frontier, Appl Therm Eng 207 (2022) 118128, https://doi.org/10.1016/j.applthermaleng.2022.118128.

[29] F. Chen, J. Wang, X. Yang, Topology optimization design and numerical analysis on cold plates for lithium-ion battery thermal management, Int J Heat Mass Transf 183 (2022) 122087, https://doi.org/10.1016/j.ijheatmasstransfer.2021.122087.

[30] X. Mo, H. Zhi, Y. Xiao, H. Hua, L. He, Topology optimization of cooling plates for battery thermal management, Int J Heat Mass Transf 178 (2021) 121612, https://doi.org/10.1016/j.ijheatmasstransfer.2021.121612.

[31] Q.Y. Yao, C.Y. Zhao, Y. Zhao, H. Wang, W. Li, Topology optimization for heat transfer enhancement in latent heat storage, Int J Therm Sci 159 (2021) 106578, https://doi.org/10.1016/j.ijthermalsci.2020.106578.

[32] T. Dbouk, A review about the engineering design of optimal heat transfer systems using topology optimization, Appl Therm Eng 112 (2017) 841–854. https://doi.org/10.1016/j.applthermaleng.2016.10.134.

[33] J.H.K. Haertel, K. Engelbrecht, B.S. Lazarov, O. Sigmund, Topology optimization of a pseudo 3D thermofluid heat sink model, Int J Heat Mass Transf 121 (2018) 1073–1088, https://doi.org/10.1016/j.ijheatmasstransfer.2018.01.078.

[34] M. Zebarjadi, Electronic cooling using thermoelectric devices, Appl Phys Lett 106 (2015) 203506, https://doi.org/10.1063/1.4921457.

[35] E.M. Dede, S.N. Joshi, F. Zhou, Topology optimization, additive layer manufacturing, and experimental testing of an air-cooled heat sink, J Mech Des 137.11 (2015) 111403, https://doi.org/10.1115/1.4030989.

[36] Lee, HoSung. Thermoelectrics: design and materials. John Wiley & Sons, 2016.

[37] R.R.J. Sélo, S. Catchpole-Smith, I. Maskery, I. Ashcroft, C. Tuck, On the thermal conductivity of AlSi10Mg and lattice structures made by laser powder bed fusion, Addit Manuf 34 (2020) 101214, https://doi.org/10.1016/j.addma.2020.101214.

[38] Laird Thermal Systems, Performance sheet, Available from: <https://www.mouser.kr/ProductDetail/739-387004946>

[39] Z. Khattak, H.M. Ali, Air cooled heat sink geometries subjected to forced flow: A critical review, Int J Heat Mass Transf 130 (2019) 141–161, https://doi.org/10.1016/j.ijheatmasstransfer.2018.08.048.

[40] G.J. Snyder, A.H. Snyder, Figure of merit ZT of a thermoelectric device defined from materials properties, Energy Environ Sci 10 (2017) 2280–2283, https://doi.org/10.1039/c7ee02007d.

[41] O. Sigmund, K. Maute, Topology optimization approaches: A comparative review, Struct Multidiscip Optim 48 (2013) 1031–1055, https://doi.org/10.1007/s00158-013-0978-6.

[42] K. Peszyński, L. Olszewski, E. Smyk, D. Perczyński, Analysis of the velocity distribution in different types of ventilation system ducts, EPJ Web Conf 180 (2018) 02081, https://doi.org/10.1051/epjconf/201818002081.

[43] Z. He, Y. Yan, Z. Zhang, Thermal management and temperature uniformity enhancement of electronic devices by micro heat sinks: A review, Energy 216 (2021) 119223, https://doi.org/10.1016/j.energy.2020.119223.

[44] Y. Wang, C. Wu, Z. Tang, X. Yang, Y. Deng, C. Su, Optimization of Fin Distribution to Improve the Temperature Uniformity of a Heat Exchanger in a Thermoelectric Generator, J Electron Mater 44 (2015) 1724–1732, https://doi.org/10.1007/s11664-014-3527-1.

[45] H. Lu, T. Wu, S. Bai, K. Xu, Y. Huang, W. Gao, et al., Experiment on thermal uniformity and pressure drop of exhaust heat exchanger for automotive thermoelectric generator, Energy 54 (2013) 372–377. https://doi.org/10.1016/j.energy.2013.02.067.

[46] S. Venko, B. Vidrih, E. Pavlovič, S. Medved, Enhanced heat transfer on thermo active cooling wall, Stroj Vestn/J Mech Eng 58 (2012) 623–632, https://doi.org/10.5545/sv-jme.2012.436.

[47] S. Choo, J. Lee, B. Şişik, S.J. Jung, K. Kim, S.E. Yang, et al., Geometric design of Cu2Se-based thermoelectric materials for enhancing power generation, Nat Energy 9.9 (2024) 1105–1116, https://doi.org/10.1038/s41560-024-01589-5.

[48] J.H. Kim, A. Yusuf, S.E. Moon, J. Pil Im, S. Ballikaya, Experimental and Theoretical Optimization of Wearable Thermoelectric Generators Based on Fill Factor and Leg Geometry, ACS Appl Energy Mater (2024), https://doi.org/10.1021/acsaem.4c01794.

[49] Y. Zhu, D.W. Newbrook, P. Dai, C.H.K. de Groot, R. Huang, Artificial neural network enabled accurate geometrical design and optimisation of thermoelectric generator, Appl Energy 305 (2022) 117800, https://doi.org/10.1016/j.apenergy.2021.117800.